INTERFACE

rsif.royalsocietypublishing.org

Research

Cite this article: Cleary JM, Lipsky ZW, Kim M, Marques CNH, German GK. 2018 Heterogeneous ceramide distributions alter spatially resolved growth of *Staphylococcus aureus* on human stratum corneum. *J. R. Soc. Interface* **15**: 20170848.
http://dx.doi.org/10.1098/rsif.2017.0848

Received: 13 November 2017
Accepted: 22 March 2018

Subject Category:
Life Sciences–Engineering interface

Subject Areas:
biomedical engineering, biophysics

Keywords:
stratum corneum, ceramide, *Staphylococcus aureus*, biofilms, sphingosine, topography

Author for correspondence:
Guy K. German
e-mail: ggerman@binghamton.edu

†These authors contributed equally to this work.

THE ROYAL SOCIETY
PUBLISHING

Heterogeneous ceramide distributions alter spatially resolved growth of *Staphylococcus aureus* on human stratum corneum

Joseph M. Cleary[1,3,†], Zachary W. Lipsky[1,3,†], Minyoung Kim[2,3], Cláudia N. H. Marques[2,3] and Guy K. German[1,3]

[1]Department of Biomedical Engineering, [2]Department of Biological Sciences, and [3]Binghamton Biofilm Research Center, Binghamton University, 4400 Vestal Parkway East, Binghamton, NY 13902, USA

GKG, 0000-0003-2872-4775

Contemporary studies have revealed dramatic changes in the diversity of bacterial microbiota between healthy and diseased skin. However, the prevailing use of swabs to extract the microorganisms has meant that only population 'snapshots' are obtained, and all spatially resolved information of bacterial growth is lost. Here we report on the temporospatial growth of *Staphylococcus aureus* on the surface of the human stratum corneum (SC); the outermost layer of skin. This bacterial species dominates bacterial populations on skin with atopic dermatitis (AD). We first establish that the distribution of ceramides naturally present in the SC is heterogeneous, and correlates with the tissue's structural topography. This distribution subsequently impacts the growth of bacterial biofilms. In the SC retaining healthy ceramide concentrations, biofilms exhibit no spatial preference for growth. By contrast, a depletion of ceramides consistent with reductions known to occur with AD enables *S. aureus* to use the patterned network of topographical canyons as a conduit for growth. The ability of ceramides to govern bacterial growth is confirmed using a topographical skin canyon analogue coated with the ceramide subcomponent D-sphingosine. Our work appears to explain the causal link between ceramide depletion and increased *S. aureus* populations that is observed in AD. It may also provide insight into disease transmission as well as improving pre-operative skin cleansing techniques.

1. Introduction

The stratum corneum (SC) is a protective barrier that is host to a diverse population of microorganisms that naturally populate the human skin surface [1]. Most microorganisms within this microbiome are harmless, however, some are opportunistic pathogens [2,3]. An increase in population of one such species, *Staphylococcus aureus* [2], has been linked to numerous skin diseases including atopic dermatitis (AD), cellulitis and impetigo [4,5]. It is also the most common cause of surgical site infections [6], which occur in 5% of all surgical operations [7]. Disparate studies have also revealed AD is associated with a depletion of SC lipids, most notably ceramides [8–11]. Ceramides are the most populous family of lipids present in and on the surface of the SC [12]. They comprise one of four different sphingoid bases and a fatty acid [13]. The most common sphingoid base is sphingosine [14,15]. Sphingosine has been shown to exhibit antimicrobial properties through its ability to disrupt the membrane of Gram-positive bacteria, such as *S. aureus*. While the exact mechanism of action is not fully understood, it is currently thought to be due to sphingoid-base insertion into the bacterial membrane, rendering the membrane non-functional or inhibiting certain key enzymes upon insertion [12,16]. Yet with this antimicrobial understanding

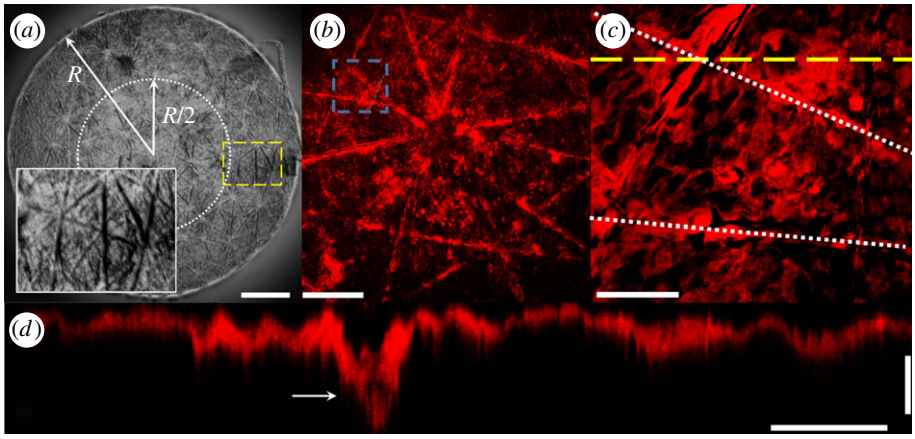

Figure 1. SC exhibits topography. (*a*) Composite transmitted light image of an isolated circular sample of human SC. Scale bar, 1 mm. (Dotted line) Inner half radius of circular, $R = 3$ mm SC sample. (Dashed line) Location of inset image highlighting topographical microchannels. (*b*) Composite fluorescent image of a BODIPY FL C_{12}-Sphingomyelin ceramide stained SC sample. Scale bar, 300 μm. (*c*) Plan view of the region outlined by the blue dashed line in *b*. Scale bar, 100 μm. (Dotted line) Location of topographical microchannel. (Yellow Dashed line) Profile view displayed in *d*. (*d*) Cross-section through a microchannel highlighting the topography, extracted from a three-dimensional confocal image stack. The arrow shows the location of the microchannel. Horizontal and vertical scale bars, 50 μm and 5 μm, respectively.

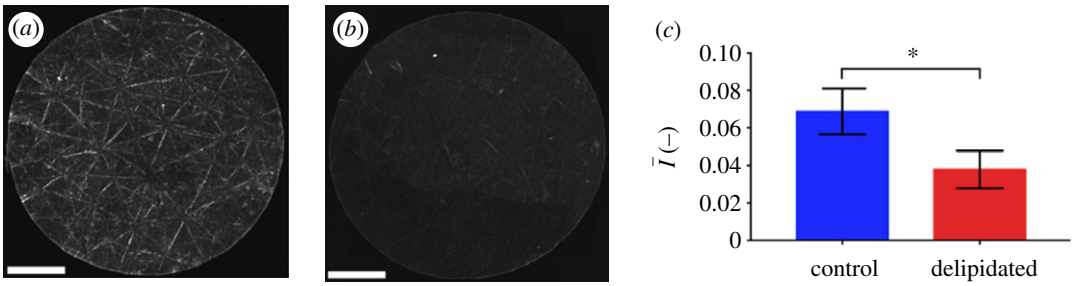

Figure 2. Global changes in SC ceramides with delipidation. (*a*,*b*) Composite fluorescent image of a BODIPY FL C_{12}-Sphingomyelin ceramide stained circular SC sample ($R = 3$ mm) retaining a normal lipid composition (*a*) and following delipidation (*b*). Scale bars, 1 mm. (*c*) Average normalized lipid fluorescence within the inner *R*/2 region of control and delipidated SC. Error bars denote the mean ± s.d. of $n = 3$ individual SC samples for each lipid condition.

revealed, little is still understood about how SC lipids might influence bacterial growth on the skin surface.

Previous studies examining skin lipid composition and microbiome diversity use swabs or solvent extraction methods to collect specimens for analysis [17–19]. Consequently, these studies are unable to capture spatially resolved bacterial and lipid distributions. Human SC is structurally heterogeneous, exhibiting a rich topography over many length scales [20]. Its most visible feature is the patterned network of open channel grooves that surround triangular corneocyte cell clusters. Lipids, in and on the SC, appear to be heterogeneously distributed due to these microchannels, with increased concentrations inside the grooves [20]. We anticipate this will impact the spatially resolved growth of bacterial biofilms. In this article, we take a first step towards understanding the interplay between lipid distributions and the dynamic growth of *S. aureus* on human SC tissue.

2. Results and discussion

2.1. Human stratum corneum exhibits topography

Brightfield microscopy of isolated human SC, shown in figure 1*a*, reveals the tissue is rich in topography, exhibiting a triangular network of microchannels. This topography is confirmed by confocal imaging SC samples stained with BODIPY Fl C_{12}-Sphingomyelin, a probe known to bind primarily to ceramides [21,22]. Fluorescent images in figure 1*b*,*c* show that the edges of the triangular cell clusters [23] appear to exhibit a more intense fluorescent response. These edges correspond with topographical canyons (figure 1*d*), which extend approximately 50–75% into the total SC thickness [24].

2.2. Human stratum corneum ceramide distributions are heterogeneous

Since free sphingoid bases are known antimicrobial agents in skin barrier function [16], and the result of ceramide metabolism [8], we hypothesize that localized regions of high ceramide concentrations, the most common class of SC lipid [13], will inhibit bacterial biofilm growth through metabolic breakdown into free sphingoid bases such as sphingosine [16]. This is evaluated by quantifying the spatially resolved growth of *S. aureus* bacteria on human SC exhibiting contrasting lipid concentrations and distributions. Lipid concentrations and distributions are first quantified under two conditions: control samples retaining high lipid concentrations and samples partially depleted of surface and intercellular lipids (including cholesterol, ceramides and free fatty acids) using a solvent extraction process [18,25–27]. Figure 2*a* and *b*, respectively, shows fluorescent images of ceramide stained control and delipidated samples from the same skin specimen.

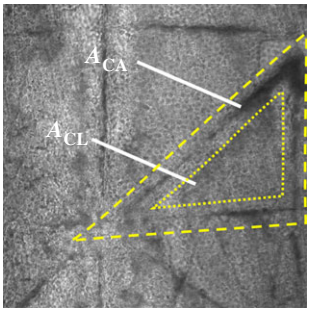

Figure 3. Characterizing regions of SC tissue. Transmitted light image of isolated human SC showing triangular subunits. The area in between the dotted and dashed line corresponds to the topographical canyon region, A_{CA}, while the region within the dotted line corresponds to the inner cluster region, A_{CL}. (Online version in colour.)

Figure 2*c* shows that delipidation results in a 45% decrease in the average normalized fluorescent intensity (NFI), $\bar{I}$, relative to controls. This decrease suggests that delipidation causes a comparable decrease in ceramides to the average decrease (35%) observed in lesional skin of AD patients [11]. To highlight spatially resolved variations in ceramide fluorescence between the two SC conditions, we distinguish between two distinct areas of the SC: topographically rich canyon regions in proximity to microchannels, and more planar regions that the microchannels surround, which we denote cluster regions. Relative fluorescent intensities within each of these regions are quantified by subdividing triangular base units of the SC [23] into two areas: an outer triangular annulus encompassing the topographical canyons, A_{CA} and an inner triangular cluster region encompassing the corneocytes that the microchannels surround, A_{CL}. A schematic of these regions is provided in figure 3. For each triangular subunit, the defined areas of the two regions are matched to within 5% in order to minimize sampling bias. Background subtracted fluorescent surface densities within the canyon and cluster regions are then, respectively, established by quantifying the expressions, $\bar{I}_{CA} = \sum I_{CA}/A_{CA}$ and $\bar{I}_{CL} = \sum_{CL}^{1}/A_{CL}$, where $\sum I$ denotes the sum of the fluorescent intensity of pixels within the area. Figure 4*a* and *b*, respectively, shows the normalized fluorescent surface densities in the canyon, $\hat{I}_{CA} = \bar{I}_{CA}/(\bar{I}_{CL} + \bar{I}_{CA})$ and cluster regions $\hat{I}_{CL} = \bar{I}_{CL}/(\bar{I}_{CL} + \bar{I}_{CA})$ of triangular base units extracted from control and delipidated SC. The control SC condition shows increased fluorescence in the canyon regions relative to the inner cluster regions (figure 4*a*), indicative of increased localized ceramide concentrations. However, delipidated SC shows a more homogeneous spatial distribution (figure 4*b*). The average difference between the normalized fluorescent surface densities in the two regions, $\overline{\hat{I}_{CA} - \hat{I}_{CL}}$, shown in figure 4*c*, confirms the delipidation process results in a more homogeneous distribution of the remaining ceramides.

2.2.1. Changes in ceramide distributions correlate with altered biofilm growth patterns

The impact of ceramide distributions on the spatio-temporal growth of *S. aureus* expressing green fluorescent protein (GFP) is assessed. Daily biofilm growth is recorded on both delipidated and control SC samples embedded in a silicone elastomer substrate. Embedding leaves only the superficial SC face exposed, preventing bacteria from growing on the tissue underside. Figure 5*a* compares the mean fractional surface area of control and lipid-depleted SC samples covered by bacteria over a 7-day period. Measurements are taken every 24 h over a 7-day period, beginning after samples are inoculated with *S. aureus* (10^8 colony forming units (CFU) ml^{-1}) for 2 h under static flow conditions to promote bacterial adhesion. In contrast to days 1–7, a greater bacterial coverage on both SC types occurs 2 h post-inoculation (denoted day 0). This is due to settlement of bacteria on the SC surface. Subsequent coverage then decreases due to media flow (8 ml h^{-1}, 5% brain–heart infusion medium (BHI) with 250 ng ml^{-1} tetracycline), washing away unbound bacteria, an observation consistent with previous findings of biofilm formation [28]. Relative to controls, delipidated SC primarily exhibits increased bacterial coverage after day 2, indicating *S. aureus* favours a lipid-depleted environment over extended periods of time. Prior to this, control SC exhibit greater bacterial coverage.

In addition to changes in population, figure 5*b–g* highlights striking differences in spatially resolved bacterial settlement and growth between the two SC lipid conditions. Figure 5*b* and *c*, respectively, shows that after a 2 h settlement period, *S. aureus* on control SC nearly exclusively avoid topographical canyons, while settlement occurs predominantly within the microchannels of delipidated SC. After 3 days, microcolonies remain small and not readily visible on either tissue type (figure 5*d*,*e*). After 7 days growth, bacterial colonization on control SC (figure 5*f*) exhibits no identifiable spatial preference for growth. By contrast, biofilm growth on delipidated SC occurs notably within the microchannels (figure 5*g*). The delipidation process removes locally high concentrations of ceramides, which contain an antimicrobial sphingosine base [12,16], from within the microchannels (figure 4*a*,*b*). This depletion appears to enable bacteria to invade (figure 5*c*) and grow (figure 5*g*) within these topographical features. The heightened bacterial growth in the microchannels also appears consistent with studies that report non-motile bacteria preferentially grow within topographical recesses [29].

Figure 6 further elucidates how changes in SC lipid concentrations influence localized biofilm colonization after 7 days of growth. The spatially resolved preference for bacterial growth inside or outside the canyons is characterized by employing the previously described process of subdividing triangular geometric units of SC. We account for three-dimensional biofilm growth by capturing confocal images of bacterial fluorescence and summing confocal image stacks over a *z*-height of 64 µm, ranging between the base of the topographical canyons and approximately 40 µm above the SC surface. This ensures all bacterial fluorescence is captured. The schematic in figure 6 outlines the range captured. Figure 6*a* highlights that while bacteria grow all over control SC, the inner cluster regions primarily exhibit increased bacterial fluorescence surface densities, $\hat{I}_{CL}$, relative to the surrounding canyons, $\hat{I}_{CA}$. By contrast, figure 6*b* shows that delipidated SC exhibits greater fluorescent surface densities within the canyons. The averaged difference in the relative fluorescent surface density between the two areas, $\overline{\hat{I}_{CA} - \hat{I}_{CL}}$, for each SC condition is shown in figure 6*c*. A statistically significant preference towards bacterial growth in canyons occurs when SC is delipidated.

A preference for bacterial growth inside of the canyons regions of lipid-depleted SC (figures 5 and 6) does not explicitly distinguish between growth inside the microchannels, or merely in proximity to the canyon edges. To discern this difference, NFI profiles perpendicular to the long axis of

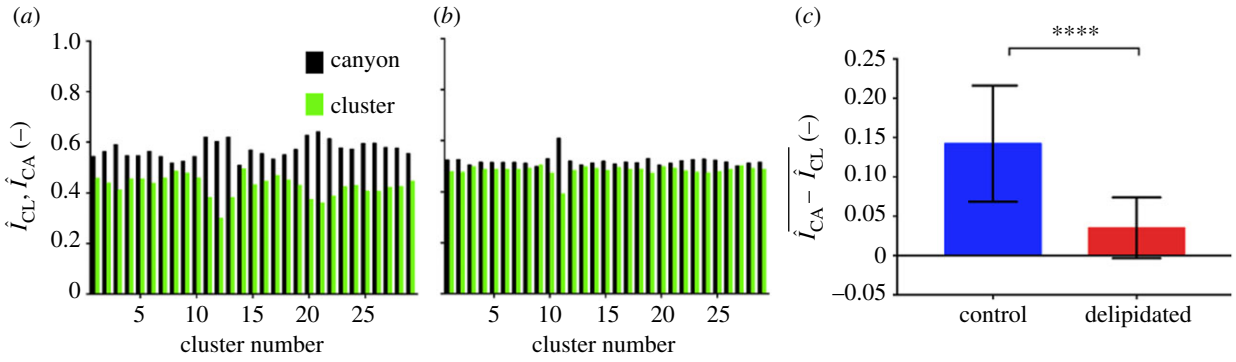

Figure 4. Locally high concentrations of ceramides in microchannels become depleted with delipidation. (*a*,*b*) Normalized fluorescent surface densities within the topographical canyons ($\hat{I}_{CA}$, black) and clusters ($\hat{I}_{CL}$, green) of control (*a*, $n = 30$ total triangular base units from $n = 3$ SC samples) and delipidated SC (*b*, $n = 30$ total triangular base units from $n = 3$ SC samples). (*c*) Averaged difference between canyon and cluster normalized fluorescent surface densities for control and delipidated SC ($n = 30$). Error bars denote the mean $\pm$ s.d. between the samples.

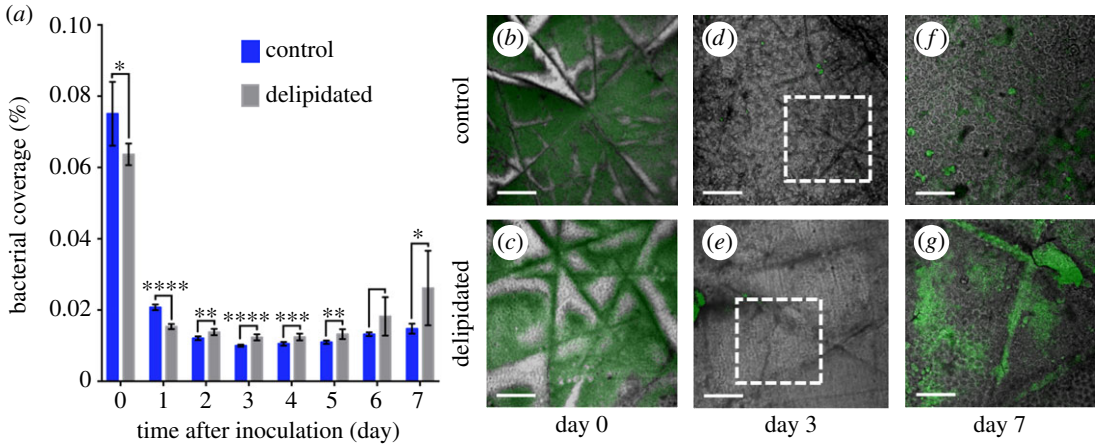

Figure 5. *Staphylococcus aureus* coverage and spatially resolved growth varies with SC lipid content. (*a*) Average fractional bacterial coverage of the same regions of control (dark blue) and lipid-depleted (light grey) SC samples over time. Error bar denotes the mean $\pm$ s.d. of $n = 2$ SC samples per lipid condition ($n = 8$ regions per SC sample). Representative images of spatially resolved bacterial colonization and biofilm growth on (top row) control and (bottom row) delipidated SC samples over time. Images comprised a transmitted light image of SC overlaid with the fluorescent bacterial emission (green). (*b*,*c*) Bacterial growth 2 h post-inoculation (denoted day 0). Scale bar, 300 µm. (*d*,*e*) Microcolony formation 3 days post-inoculation. Scale bar, 300 µm. (*f*,*g*) Biofilm formation 7 days post-inoculation. These images, respectively, correspond to regions outlines in *d* and *e*. Scale bar, 150 µm.

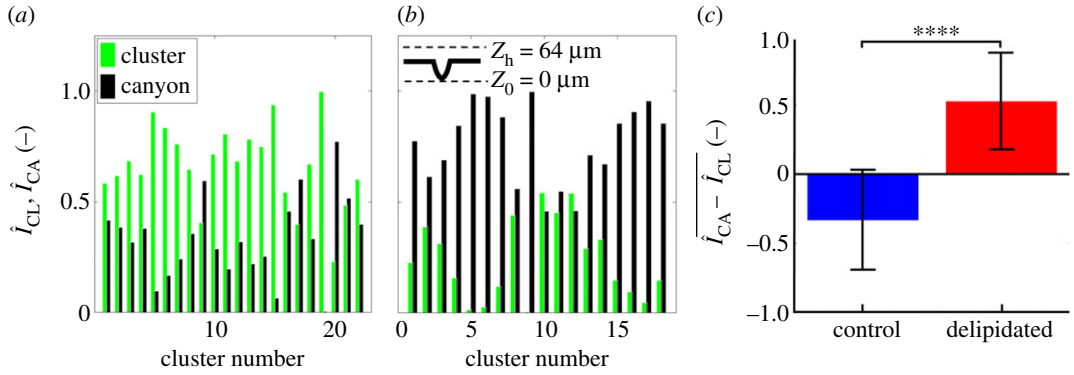

Figure 6. Delipidation enables preferential *S. aureus* growth in and near microchannels. (*a*,*b*) Normalized fluorescent surface density of *S. aureus* in the topographical canyons ($\hat{I}_{CA}$, black) and clusters ($\hat{I}_{CL}$, green) of (*a*) control (*b*) delipidated SC. The schematic at the top of *b* describes the range over which fluorescent information is gathered. Here, Z_0 denotes the bottom of the canyon, and Z_h denotes the maximum height at which bacterial fluorescence is summed. (*c*) Averaged difference between canyon and cluster normalized fluorescent surface densities for control and delipidated SC. Error bars denote the mean $\pm$ s.d. between the samples (control) $n = 22$ assessments from $n = 3$ SC samples; (lipid depleted) $n = 18$ assessments from $n = 3$ SC samples.

microchannels are captured over time using confocal microscopy for the control and delipidated SC conditions. Representative NFI profiles for control and delipidated SC are, respectively, shown in figure 7*a* and *b*. The intensity profile for each day is normalized by the peak recorded intensity over the entire 7-day period. After 2 h of bacterial settlement (denoted day 0), control SC fluoresces at all locations along the profile, exhibits a peak outside of the canyon edge, and a

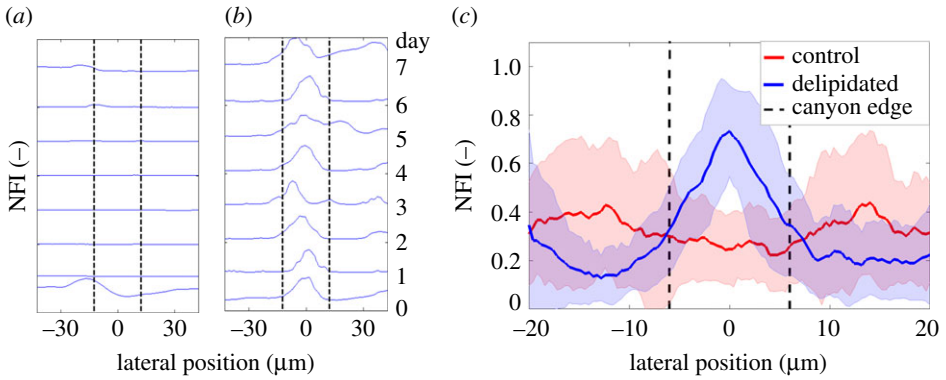

Figure 7. *Staphylococcus aureus* biofilms preferentially grow within delipidated SC microchannels. (*a*,*b*) Normalized bacterial fluorescence intensity profiles across the same topographical canyon of (*a*) control and (*b*) delipidated SC over time. For each lipid condition, each profile is normalized by the peak fluorescent intensity over the 7 day cycle. (Vertical black dashed line) Edge of the topographical canyon. (*c*) Average normalized bacterial fluorescence profile across topographical canyons 7 days following *S. aureus* inoculation. (Red solid line) Control SC ($n = 4$ SC samples, $n = 358$ canyon profiles). (Blue dashed line) Delipidated SC ($n = 4$ SC samples, $n = 408$ canyon profiles). Shaded regions surrounding the lines denote the standard deviation. (Vertical black dashed lines) Average width of the topographical canyons.

minimum within the canyon (figure 7*a*). After day 6, biofilms are present at the canyon edge, but do not notably invade the canyon. Bacterial fluorescence is also present at all locations across the cross-sectional profile of a delipidated SC microchannel 2 h after inoculation (figure 7*b*), however, a clear peak is visible within the canyon. This peak persists throughout the 7 days, indicating bacterial populations do not diminish. After 7 days of growth, biofilms remain primarily within the microchannel, but are not laterally confined by the canyon edges.

Figure 7*c* compares the average NFI profiles across multiple canyons in control SC (red, $n = 358$ individual cross sections from $n = 4$ SC samples) and delipidated SC (blue, $n = 408$ individual cross sections from $n = 4$ SC samples) after 7 days of bacterial growth. Prior to averaging, each profile is normalized by its peak fluorescent intensity. The control SC profile remains non-zero and near constant across the canyon, indicating no spatial preference for growth. By contrast, the delipidated SC profile shows a distinct peak midway across the canyon, indicating a clear spatial preference for biofilm growth directly at the base of the microchannel.

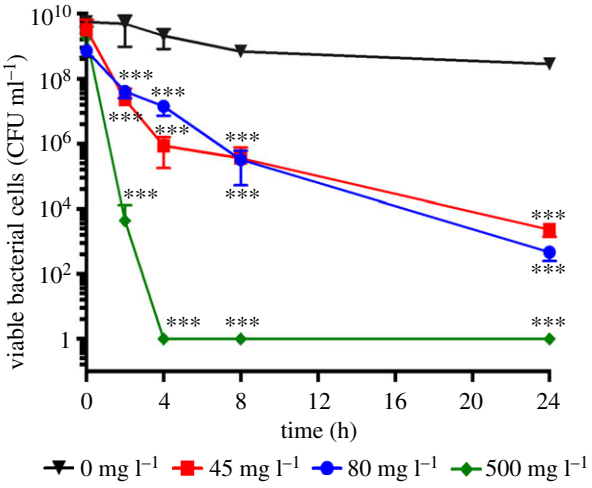

Figure 8. Time–kill curves of *S. aureus* exposed to D-sphingosine. Average ($n = 4$) cell viability of *S. aureus* mid-exponential phase planktonic cultures in BHI exposed to (inverted triangle) 0 mg l^{-1}, (square) 45 mg l^{-1}, (circle) 80 mg l^{-1} and (diamond) 500 mg l^{-1} of D-sphingosine in DMSO over a 24-h period. Error bars denote standard deviations. Statistical significance with respect to controls is established using a one-way ANOVA. (Online version in colour.)

2.2.2. Sphingosine coating of an analogue skin canyon model impedes bacterial biofilm growth

While the delipidation protocol we employ removes ceramides, cholesterol and free fatty acids from the SC [25], we anticipate the depletion of localized high concentrations of antibacterial ceramides from within the canyons enables greater localized *S. aureus* biofilm growth. To test this, the antibacterial effect of coating an analogue SC canyon (width 820 ± 29 μm, height 424 ± 24 μm) with the ceramide subcomponent sphingosine is quantified. The antibacterial properties of the synthetic D-sphingosine used for the study are first assessed *in vitro*. The minimum inhibitory concentration is greater than 50 mg l^{-1}, while the minimum bactericidal concentration is 500 mg l^{-1}. Figure 8 shows that exposure of exponential phase planktonic *S. aureus* to D-sphingosine results in a 7-log reduction in cell viability at low concentrations of 45 and 80 mg l^{-1}, and eradication after a 4 h exposure to a 500 mg l^{-1} concentration.

The canyon region of the analogue substrates are coated with a thin solid film of either dimethyl sulfoxide (DMSO) alone, or D-sphingosine dissolved in DMSO (SPH, 500 mg l^{-1}). Analysis of channel cross-sectional profiles reveals no notable differences in shape or channel roughness between the two types of coating, based on measurements of average (Ra) and root mean square roughness (Rq) [30] obtained through optical profilometry (DMSO: $Ra = 67.5 \pm 37.5$ nm, $Rq = 91.5 \pm 44.0$ nm ($n = 2$ substrates), SPH: $Ra = 91.4 \pm 30.6$ nm, $Rq = 118.4 \pm 106.9$ nm ($n = 2$ substrates)). Using a flow cell as with previous experiments, substrates are inoculated with 10^8 CFU ml^{-1} of *S. aureus*, allowed to attach to the substrate for 2 h under static conditions, and then imaged daily for 8 days. Composite confocal images of daily bacterial fluorescence on $n = 2$ DMSO-coated analogue substrates and $n = 2$ SPH-coated substrates are shown in figure 9. Clear differences in the fluorescent intensity between the canyons with and without the sphingosine coating are evident, in particular, for the 54, 98 and 122 h time points. Figure 10 plots the summed fluorescent surface density of GFP-labelled *S. aureus*, $\bar{I}_{CA} = \sum I_{CA}/A_{CA}$, within both canyon types ($n = 2$

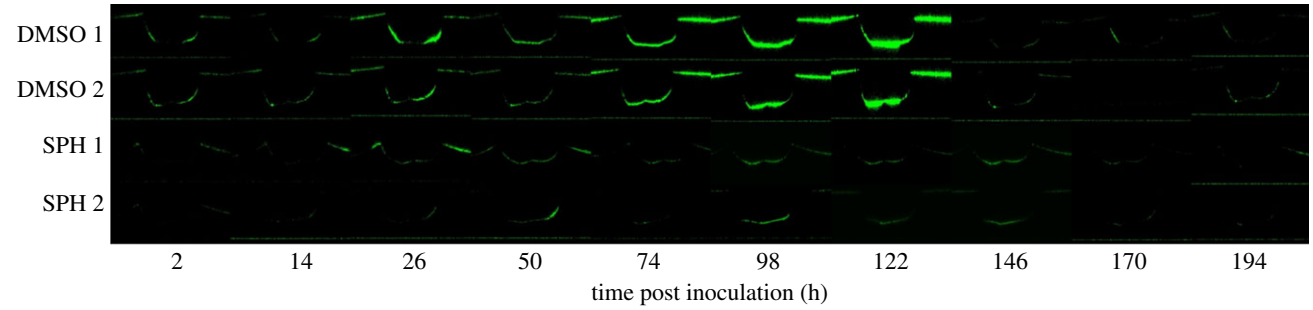

Figure 9. Cross-sectional confocal composite fluorescent images of bacteria within a skin canyon analogue. Representative fluorescent cross sections (1550 × 500 μm) of GFP-labelled *S. aureus* bacteria within a silicone elastomer topographical canyon analogue over time. An identical contrast change has been imposed on all images to enhance visual clarity. (Rows 1 and 2) Two different canyons coated with a desiccated film of DMSO. (Rows 3 and 4) Two different canyons coated with a desiccated film of DMSO containing 500 mg l^{-1} D-sphingosine. Original unaltered images are used to establish results shown in figure 10.

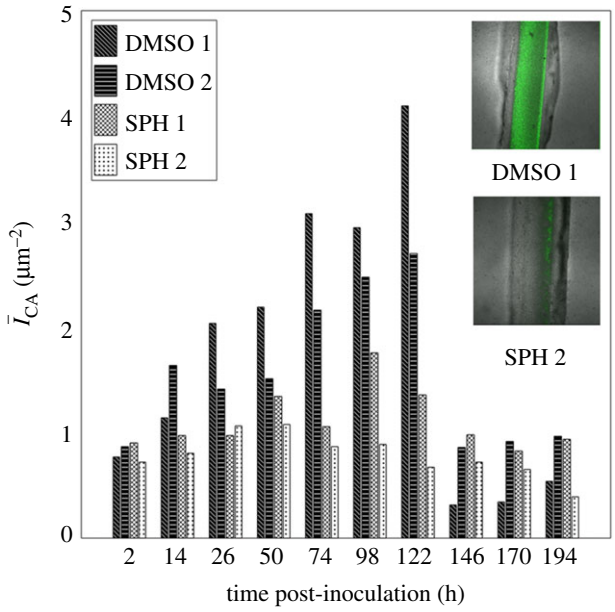

Figure 10. D-sphingosine coatings reduce bacterial growth within analogue microchannels. Fluorescent surface density, $\bar{I}_{CA}$, of GFP-labelled *S. aureus* bacteria within an analogue topographical canyon (820 ± 29 μm wide, 424 ± 24 μm deep) measured over an 8-day period. Canyon surfaces are coated with dried films of DMSO (DMSO, black with slanted or horizontal lines) or D-sphingosine in DMSO (SPH, 500 mg l^{-1}, white with cross or dot pattern). The inset images show representative transmitted light images of DMSO (DMSO 1)- and sphingosine with DMSO (SPH 2)-coated canyons overlaid with bacterial fluorescent emissions at a height of 170–172 μm from the base of each canyon, after 122 h growth.

for each coating) over an 8-day period, beginning after a 2 h inoculation period. As previously detailed, we account for three-dimensional biofilm growth by summing confocal image stacks over a *z*-height of 500 μm (2 μm intervals), ranging between the base of the canyon and substrate surface. For each canyon and time point analysed, A_{CA}, corresponds to the product of the canyon width and a fixed length of 1550 μm along the long axis of each canyon. Over the first 122 h, canyons coated only with DMSO show a monotonic increase in fluorescent density, while canyons coated with DMSO and sphingosine exhibit near constant values. Canyons coated only with DMSO exhibit bacterial growth strikingly similar to those observed for the delipidated SC (figures 5 and 6). By contrast, canyons coated with films containing sphingosine exhibit bacterial growth consistent with control SC. For this latter comparison, bacterial fluorescence is not completely eliminated in either the SC or analogue canyons, but the ability of bacteria to grow is inhibited. The inset images in figure 10 show representative transmitted light images of DMSO- and SPH-coated canyons overlaid with bacterial fluorescent emissions at a height midway between the surface and base of each canyon, after 122 h growth. These figures confirm clear differences in bacterial growth, with reduced bacterial presence in the SPG coated canyons. A significant reduction in fluorescence is observed at 146 h post-inoculation for both film coatings. We anticipate this is due to dispersal typically seen with biofilms under flow conditions [31].

In this article, we highlight that human SC ceramides [32,33] are heterogeneously distributed, with increased concentrations found within topographical microchannels (figures 2 and 4). When SC is partially depleted of lipids [25], these increased concentrations are lost (figure 4*b*). The ability of sphingosine in ceramides to impart antimicrobial properties to the skin surface [12,16] suggests that localized ceramide depletion enables *S. aureus* to invade (figure 5*c*), and preferentially grow within the microchannels (figures 6 and 7), resulting in increased bacterial coverage (figure 5*a*). The avoidance of flow-induced shear forces that would act to debond bacteria is unlikely to be the cause of this preferential microchannel growth. Approximating the system as a simplified Poiseuille flow, a fluid volume flow rate of $Q = 8$ ml h^{-1} (with a dynamic viscosity of $\mu \sim 0.001$ Pa s) within the FC81 flow cell reactor (of dimensions: 50 mm long, $W = 13$ mm wide and $H = 2.35$ mm tall), would induce a wall shear stress, $\tau_W = 6\,\mu Q\,(WH^2)^{-1}$, of approximately 10^{-4} Pa. The shear force imposed on a single *S. aureus* bacterium (of dimension $L \sim 1$ μm [34]) would, therefore, be $F \sim \tau_W L^2 \sim 10^{-16}$ N. Adhesion bonds of *S. aureus* have been quantified to be approximately 1.2 nN [35], seven orders of magnitude greater than the fluid induced wall forces. As such, flow-induced bacterial debonding is unlikely to occur anywhere on the skin surface. The cause of the preferential growth, therefore, remains unclear. However, non-motile bacteria, like *S. aureus*, have been shown to be capable of growing readily in microchannels [36]. Recent evidence has also shown that *S. aureus* grown on PDMS substrates with topographical features exhibit a preference for growth in recessed channels [29]. This behaviour is consistent with our observed findings for both DMSO analogue substrates and lipid-depleted SC. A potential cause of this preferential microchannel growth may be the increased cell–substrate contact area on the curved microchannel surfaces promoting stronger bacterial attachment [37,38].

Our results may help explain the causal link between reduced skin ceramides and increased colonization of the skin surface with *S. aureus* bacteria in AD [8,10,39]. Still, the cause of the heterogeneous ceramide distributions remains unclear. We anticipate skin lipids are transported and deposited by spreading sebum. Previous studies have shown that SC microchannels enable surface transport of oils via capillary wicking [40]. Topically applied ceramides also accumulate within these microchannels [41]. Future studies should consider how the heterogeneous composition and topography of the skin barrier may alter the localized microbiome population diversity and co-localization. Our results also have implications for the onset of surgical site infections. Preparation procedures that do not fully remove *S. aureus* bacteria from within topographical microchannels may result in bacterial entrainment during incision, which could cause subsequent infections of the underlying tissue.

3. Limitations

The results of this work highlight that decreased concentrations of lipids alters the spatially resolved growth of *S. aureus* bacteria on human SC. The delipidation process partially depletes all lipid types from SC [18,25–27] and appears (figure 2*c*) to reduce ceramides to levels similar to those found in lesional skin of patients with AD [11]. This is, however, based on an indirect method of ceramide quantification. The overall compositional changes may not be fully representative of AD conditions. Moreover, this work employs a standard biofilm growth methodology [42,43], which does not simulate physiologically relevant conditions; skin is not continually immersed in nutrients or water throughout the day. *In vivo*, bacteria will survive on skin using nutrients available, including lipids and keratin [44].

This work compares changes in bacterial growth with ceramide concentrations and distributions. Changes in bacterial growth within analogue microchannels due to a coating of the ceramide subcomponent sphingosine supports our hypothesis that ceramides are the primary cause of changes in bacterial growth. However, the impact of other lipid types that may provide additional antimicrobial properties have not been examined here and should be analysed in future studies. Finally, the *S. aureus* ALC2085 strain [45] used for this study differs from the strains found on human skin with AD and has recently been shown to have reduced expression of several virulence genes [46]. However, this strain forms normal biofilms and has previously been used for testing antimicrobial efficacy against biofilms [47–49]. Therefore, the results of this work highlight a potential causal relationship between increased *S. aureus* populations and decreased ceramide levels with AD.

4. Material and methods

4.1. Stratum corneum isolation

Full-thickness skin specimens (31 years, female breast; 51 years, female breast) were received from Yale Pathology Tissue Services (New Haven, CT) within 24 h of elective surgery. An exempt approval (3002–13) was obtained to perform research using de-identified tissue samples pursuant to the Department of Health and Human Services regulations, 45 CFR 46.101 : b : 4. The SC was isolated using standard heat bath and trypsin techniques [50]. Once isolated, SC sheets were placed on plastic mesh, rinsed in deionized water (DIW) and dried at 23°C for 48 h at 40% relative humidity (R.H.). After drying, the outermost face of the SC was marked with an indelible marker. Marked regions of the tissue were not used for lipid or bacterial quantification studies. All studies were performed using both tissue specimens.

4.2. Stratum corneum delipidation

Each SC sheet was divided equally. One half was immersed in DIW for 60 min, a treatment that does not deplete lipids, nor irreversibly alter the intercellular lipid structure [51]. The other half was immersed in a mixture of chloroform and methanol (2 : 1 by volume, Sigma-Aldrich, St Louis, MO) for 60 min, followed by DIW for 60 min. The solvent treatment partially depletes intercellular ceramides, cholesterol and free fatty acids found in the SC [25]. Based on estimates of human SC ceramide concentrations and composition [26,52,53], treatments using similar solvent extraction protocols on human and porcine SCs [18,26,27,54] appear to reduce ceramides by 17–58%. Individual SC samples were cut from both control and delipidated SC tissue sheets using a 6 mm diameter circular hole punch (Harris Uni-Core, Redding, CA).

4.3. Imaging stratum corneum ceramides

Control and delipidated SC samples were stained with BODIPY FL C_{12}-Sphingomyelin fluorescent ceramide dye (Thermo Fisher Scientific, Waltham, MA). A 100 µl solution of 0.6 mg ml^{-1} dye in ethyl alcohol was dissolved in 1 ml of carbonate buffer (pH = 10). SC samples were then immersed in the solution for 60 s, then rinsed with citric buffer (pH = 5.5). After staining, samples were laminated to a glass coverslip and allowed to dry for 24 h [55]. SC samples were then imaged using an Eclipse Ti-U inverted microscope (Nikon, Melville, NY) with 10× objective lens (Nikon Plan UW). Each sample was excited using a SOLA 6-LCR-SB (Lumencor, Beaverton, OR) and FITC filter (503–550 nm band-pass) with an exposure time of 8 ms. Fluorescent and transmitted light images were recorded using a digital CCD camera (Andor Clara, Belfast, Northern Ireland) at a resolution of 1392 × 1040 pixels. The spatial resolution of each image was 0.65 µm pixel^{-1}. High-resolution composite images of each SC sample were obtained by recording and stitching together 120 individual images (12 × 10 grid) using an automated x–y stage and Nikon Elements software.

4.4. Quantifying average normalized ceramide fluorescence

Ceramide fluorescence was characterized by summing the fluorescent intensity within the inner half radius ($R/2$) of a circular SC sample ($R = 3$ mm, figure 1*a*), subtracting the average background fluorescent intensity outside of the sample perimeter, and normalizing this value by the sum of the saturated pixel intensity (maximum 16 384 for a 12 bit image) of the same area. For each lipid condition, the average NFI, $\bar{I}$, was established from $n = 3$ individual SC samples.

4.5. Substrate preparation

A silicone elastomer was prepared by mixing a base (Sylgard 184, Dow Corning, Midland, MI) with the curing agent in a weight ratio of 5 : 1. After mixing and degassing, the mixture was spin coated (WS-400B-6NNP/LITE, Laurell Technologies Corporation, North Wales, PA) onto a glass coverslip at 3500 r.p.m. for 3 min. The elastomer was then cured in an oven at 60°C for 12 h. This produced a silicone elastomer film with a thickness of approximately 40 µm. Fluorescent microspheres (200 nm, 625/645 nm, ThermoFisher Scientific, Waltham, MA) were chemically deposited onto the elastomer substrate through well-established chemical bonding techniques [56,57]. A second elastomer layer was then spin coated on top of the substrate using an identical protocol. Prior to curing, control and lipid-depleted SC samples were alternately embedded in the uncured elastomer along the centreline of the coverslip,

leaving only their outermost face exposed. The elastomer was then cured at 23°C and 40% R.H. for 24 h. This embedding process occludes the sides and underside of the SC sample, preventing bacterial growth in these regions. For each substrate tested, the order of the conditioned SC samples deposited was randomized.

4.6. Bacterial strains

All bacterial studies used *S. aureus* ALC2085 (strain RN6390 containing *pALC2084)*, constitutively expressing GFP [45]. Overnight cultures were grown in BHI media (Becton, Dickinson, Sparks, MD) supplemented with 10 mg l^{-1} chloramphenicol (Mediatech, Corning Life Sciences, Corning, NY) for plasmid maintenance, and 250 ng ml^{-1} tetracycline (Amresco, Solon, OH) for induction of green fluorescence protein (GFP), in Erlenmeyer flasks at 37°C with agitation (220 r.p.m.).

4.7. Biofilm cultures

Embedded SC samples were sterilized under ultraviolet light for 15 min, then mounted in an anodized aluminium flow cell reactor (FC81, BioSurface Technologies Corp., Bozeman, MN). The flow cell was inverted to prevent gravitational sedimentation of bacteria onto the SC samples, connected to an inlet carboy containing 5% BHI medium (Franklin Lakes, NJ) and an outlet carboy via silicone tubing. The medium was supplemented with 250 ng ml^{-1} tetracycline hydrochloride (Amresco) for induction of GFP. The closed system was maintained in equilibrium with atmospheric pressure using a gas permeable filter (200 nm pore size) fitted to each vessel. The flow cell reactor was then perfused with the media at 8 ml h^{-1}, and subsequently inoculated with 5 ml of a stationary phase culture of *S. aureus* (10^8 CFU ml^{-1}), grown in tetracycline (250 mg l^{-1}) and chloramphenicol (10 mg l^{-1}) supplemented BHI. *S. aureus* was allowed to attach to the substrate for 2 h under static conditions before laminar flow was reinstated [43,58].

4.8. Microscopic imaging of bacterial colonization of stratum corneum

Staphylococcus aureus biofilm development was monitored using fluorescence microscopy for a period of up to 7 days. *Epifluorescence microscopy:* images were acquired using an inverted microscope with 10× objective lens. Fluorescent beads were excited using a SOLA lamp with TRITC filter (590–650 nm bandpass) and imaged using an exposure time of 1.5 s. *Staphylococcus aureus* bacteria were excited using the same lamp with FITC filter, and imaged with an exposure time of 1.5 s. An automated x–y stage was employed to record multiple regions. *Confocal microscopy:* images were acquired using a confocal microscope (Leica SP5, Wetzlar, Germany) with 10, 20 and 40× objective lens; respectively, with spatial resolutions of 1.51, 0.76 and 0.38 µm px^{-1}, and numerical apertures of 0.4, 0.7 and 1.25. SC samples were illuminated sequentially with transmitted light, 455 and 633 nm wavelength lasers. Transmitted light images were used to distinguish topographical regions of the SC. The 455 nm illumination was used to excite GFP-tagged *S. aureus*. The 633 nm illumination was used to excite the fluorescent particles embedded in the elastomer substrate. At each recorded time point, z-stack images were recorded across the full depth of the SC sample and substrate at height increments of 1.33 µm. Images of the same region of each SC sample were recorded every 24 h for 7 days. This was achieved by matching the distribution of fluorescent particles during imaging with those of the previous day.

4.9. Quantifying bacterial coverage

Fluorescent images of the same regions of a SC sample were captured every 24 h using the Nikon Ti-U microscope with 10× objective lens ($n = 8$ regions per SC samples, $n = 2$ individual SC samples per lipid condition). Bacterial coverage of each sample was quantified through binary classification. Pixels exceeding 25% of the maximum bit intensity (an intensity of 4096 or greater) are counted. Fractional coverage for each region was then quantified by scaling the total number of counted pixels by the total number of pixels within each image (1392 × 1040 pixels). For each lipid condition, the eight individual fractional coverage values recorded for each day were then used to establish the mean daily fractional coverage and standard deviation.

4.10. Characterizing spatially resolved ceramide and *Staphylococcus aureus* fluorescence

The microchannel network was used to divide the SC surface into two regions: canyon regions located in proximity to the microchannels, and more planar regions that the microchannels surround, which we denote cluster regions. Figure 3 shows an example of this division. The region surrounded by the dotted line corresponds to the inner cluster area, A_{CL}, whereas the outer dashed line and inner dotted line demark the surrounding canyon area, A_{CA}. An algorithm was used to area-match these two regions to minimize sampling bias. This was achieved by manually selecting the three vertices of the triangular feature, then incrementally expanding or eroding the inner dotted boundary and outer dashed boundary by 1 px until the areas agreed to within 5%.

4.11. Quantifying minimum inhibitory and bactericidal concentrations of D-sphingosine

The minimum inhibitory concentration of D-sphingosine on *S. aureus*, established using BHI medium and a standard methodology [59,60], was greater than or equal to 100 mg l^{-1}. The minimum bactericidal concentration was also established to be equal or greater than 500 mg l^{-1}.

4.12. Quantifying time–kill curves

The effect of synthetic D-sphingosine on mid-exponential phase cultures of *S. aureus* was established using time–kill curve assays. D-sphingosine dissolved in DMSO was used to supplement mid-stationary phase cultures of *S. aureus*, grown in BHI. The final concentrations of D-sphingosine were 45, 80 and 500 mg l^{-1}. All antimicrobial exposures and controls contained an equal concentration of DMSO. *Staphylococcus aureus* cell viability was assessed over 24 h (figure 8). Relative to the control (0 mg l^{-1} D-sphingosine), a 6–7-log reduction was observed following 24-h exposure to D-sphingosine concentrations of 45 and 80 mg l^{-1}. *S. aureus* was eradicated after 4 h exposure to a D-sphingosine concentration of 500 mg l^{-1}.

4.13. Fabrication of analogue skin canyon model

A glass coverslip was placed into a custom made aluminium tray with inner dimensions 50 × 13 mm and a lip height of 2.35 mm. The coverslip formed the chamber floor. A silicone elastomer was then prepared by mixing Sylgard 184 base with its curing agent in a weight ratio of 5 : 1. After mixing and degassing, 0.5 ml was added to the chamber base and allowed to settle for 30 min. The chamber edges were coated with 40 µl of glycerol (Alfa Aesar, Haverhill, MA) prior to adding the mixture to prevent the elastomer adhering to the metal. The chamber was then placed into an oven at 60°C for 10 min. A rectangular metal rod (cross-section 0.30 × 0.50 mm) dipped in glycerol was then deposited on the semi-cured elastomer substrate with the rod aligned perpendicular to the substrate long axis. After curing in the oven for a further 4 h, the rod was removed, leaving a permanent 820 ± 29 µm wide, 424 ± 24 µm tall indentation in the elastomer film. Once rinsed

in DIW and dried, 30 µl of either DMSO (Amresco) or synthetic D-sphingosine (Sigma-Aldrich) dissolved in DMSO (500 mg l^{-1}) was then pipetted into the topographical canyon. The substrates were then desiccated under vacuum for 18 h.

4.14. Calculating roughness of coatings

A glass coverslip was spin coated with a thin flat layer of PDMS at a 5 : 1 ratio and allowed to cure at 60°C for 4 h. Thirty microlitres of DMSO or D-Sphingosine dissolved in DMSO (500 mg l^{-1}) was pipetted onto separate sections of the substrate and desiccated under vacuum for 18 h. After desiccation, profilometry was performed using a Veeco Wyko NT1100 optical profiler with 5× objective lens. The device has a vertical resolution of less than 1 nm and lateral resolution of 0.08 µm. Coatings for $n = 2$ substrates of DMSO or D-sphingosine dissolved in DMSO were measured to obtain the average roughness (*Ra*) and root mean square roughness (*Rq*) for a 1.2 × 0.94 mm region.

4.15. Imaging bacterial growth on analogue skin canyon model

Topographical substrates were placed into a flow cell reactor and inoculated with GFP-tagged *S. aureus* (10^8 CFU ml^{-1}). Fluorescent confocal *z*-stack images of canyons (2 µm interval; 500 µm total *z*-depth) were recorded using a 10× objective lens after a 2 h inoculation period in static conditions, then at 12 h, 24 h and increments of 24 h thereafter until 194 h.

4.16. Quantifying fluorescent surface density of bacterial growth in analogue skin canyons

For each canyon and time point, *z*-stacks were re-sliced using ImageJ into individual canyon cross-section profiles; each profile perpendicular to the long axis of the canyon. Representative cross sections for each canyon coating and time point are provided in figure 9. Here, the same cross-sectional profiles are shown over time for each canyon coating. In order to quantify fluorescent surface densities of GFP-labelled *S. aureus*, image intensities are first summed over the *z*-height 9 ± 6 µm below the base of the canyon to 6 ± 3 µm above the surface of the substrate within a volume defined by the canyon width and a fixed 1550 µm length along each canyon. This collective intensity is then scaled by the canyon length and width. The canyon width for each profile is measured as the lateral distance between the two canyon sides. The side of a canyon is defined as where the canyon profile deviates from horizontal. This process is repeated for all time points.

4.17. Statistical analysis

Welch's *T*-test was used to test for statistical significance in figures 2*c*, 4*c*, 5*a* and 6*c*. A one-way ANOVA was used to test for statistical significance in figure 8. Statistical analyses were all performed using GraphPad Prism V 6.0a. In the figures, $^{*}p \leq 0.05$, $^{**}p \leq 0.01$, $^{***}p \leq 0.001$ and $^{****}p \leq 0.0001$.

Data accessibility. The experimental datasets supporting this article are included in the main paper. Additional data related to this paper may be requested from the authors.

Authors' contributions. G.K.G. and C.N.H.M. conceived the idea. J.M.C., Z.L. and M.K. carried out the experiments. Everyone contributed to writing the manuscript. Revisions were completed by G.K.G., Z.L. and C.N.H.M.

Competing interests. The authors state no conflict of interest.

Funding. This material is based upon work supported by the National Science Foundation under grant no. 1653071. This work was additionally funded by Binghamton University Interdisciplinary Collaboration Grants Program, Health Sciences (TAE) award no. 66761.

Acknowledgements. The authors thank the reviewers for their valuable contributions to the revision of the manuscript.

References

1. Huttenhower C *et al.* 2012 Structure, function and diversity of the healthy human microbiome. *Nature* **486**, 207–214. (doi:10.1038/nature11234)
2. Grice EA, Segre JA. 2011 The skin microbiome. *Nat. Rev. Microbiol.* **9**, 244–253. (doi:10.1038/nrmicro2537)
3. Coates R, Moran J, Horsburgh MJ. 2014 Staphylococci: colonizers and pathogens of human skin. *Future Microbiol.* **9**, 75–91. (doi:10.2217/fmb.13.145)
4. Chiller K, Selkin BA, Murakawa GJ. 2001 Skin microflora and bacterial infections of the skin. *J. Investig. Dermatol. Symp. Proc.* **6**, 170–174. (doi:10.1046/j.0022-202x.2001.00043.x)
5. Iwatsuki K, Yamasaki O, Morizane S, Oono T. 2006 Staphylococcal cutaneous infections: invasion, evasion and aggression. *J. Dermatol. Sci.* **42**, 203–214. (doi:10.1016/j.jdermsci.2006.03.011)
6. Anderson DJ. 2011 Surgical site infections. *Infect. Dis. Clin. North Am.* **25**, 135–153. (doi:10.1016/j.idc.2010.11.004)
7. Leaper DJ. 2010 Surgical-site infection. *Br. J. Surg.* **97**, 1601–1602. (doi:10.1002/bjs.7275)
8. Arikawa J, Ishibashi M, Kawashima M, Takagi Y, Ichikawa Y, Imokawa G. 2002 Decreased levels of sphingosine, a natural antimicrobial agent, may be associated with vulnerability of the stratum corneum from patients with atopic dermatitis to colonization by *Staphylococcus aureus*. *J. Invest. Dermatol.* **119**, 433–439. (doi:10.1046/j.1523-1747.2002.01846.x)
9. Feingold KR. 2007 Thematic review series: skin lipids. The role of epidermal lipids in cutaneous permeability barrier homeostasis. *J. Lipid Res.* **48**, 2531–2546. (doi:10.1194/jlr.R700013-JLR200)
10. Imokawa G, Ishida K. 2014 Role of ceramide in the barrier function of the stratum corneum, implications for the pathogenesis of atopic dermatitis. *J. Clin. Exp. Dermatol. Res.* **5**, 1–12. (doi:10.4172/2155-9554.1000206)
11. Imokawa GL, Abe A, Jin K, Higaki Y, Kawashima M, Hidano A. 1991 Decreased level of ceramides in stratum corneum of atopic dermatitis: an etiologic factor in atopic dry skin? *J. Invest. Dermatol.* **96**, 523–526. (doi:10.1111/1523-1747.ep12470233)
12. Drake DR, Brogden KA, Dawson D V, Wertz PW, Drake DR, Dawson D V, Wertz PW. 2008 Thematic review series: skin lipids. Antimicrobial lipids at the skin surface. *J. Lipid Res.* **49**, 4–11. (doi:10.1194/jlr.R700016-JLR200)
13. Masukawa Y *et al.* 2008 Characterization of overall ceramide species in human stratum corneum. *J. Lipid Res.* **49**, 1466–1476. (doi:10.1194/jlr.M800014-JLR200)
14. Pruett ST, Bushnev A, Hagedorn K, Adiga M, Haynes CA, Sullards MC, Liotta DC, Merrill AH. 2008 *Thematic review series: sphingolipids*. Biodiversity of sphingoid bases (sphingosines) and related amino alcohols. *J. Lipid Res.* **49**, 1621–1639. (doi:10.1194/jlr.R800012-JLR200)
15. Merrill AH. 2011 Sphingolipid and glycosphingolipid metabolic pathways in the era of sphingolipidomics. *Chem. Rev.* **111**, 6387–6422. (doi:10.1021/cr2002917)
16. Fischer CL, Walters KS, Drake DR, Blanchette DR, Dawson DV, Brogden KA, Wertz PW. 2012 Sphingoid bases are taken up by *Escherichia coli* and *Staphylococcus aureus* and induce ultrastructural damage. *Skin Pharmacol. Physiol.* **26**, 36–44. (doi:10.1159/000343175)
17. Kong HH *et al.* 2012 Temporal shifts in the skin microbiome associated with disease flares and treatment in children with atopic dermatitis. *Genome Res.* **22**, 850–859. (doi:10.1101/gr.131029.111)
18. Lampe MA, Burlingame AL, Whitney J, Williams ML, Brown BE, Roitman E, Elias PM. 1983 Human stratum corneum lipids: characterization and regional variations. *J. Lipid Res.* **24**, 120–130.
19. Saint Léger D, François AM, Lévêque JL, Stoudemayer TJ, Grove GL, Kligman AM. 1988 Age-associated changes in stratum corneum lipids and

their relation to dryness. *Dermatologica* **177**, 159–164. (doi:10.1159/000248535)

20. Liu X, Cleary J, German GK. 2016 The global mechanical properties and multi-scale failure mechanics of heterogeneous human stratum corneum. *Acta Biomater.* **43**, 78–87. (doi:10.1016/j.actbio.2016.07.028)
21. Pankova-Kholmyansky I, Dagan A, Gold D, Zaslavsky Z, Skutelsky E, Gatt S, Flescher E. 2003 Ceramide mediates growth inhibition of the *Plasmodium falciparum* parasite. *Cell. Mol. Life Sci.* **60**, 577–587. (doi:10.1007/s000180300049)
22. Chu FE, Soudant P, Volety a K, Huang Y. 2000 Uptake and interconversion of fluorescent lipid analogs in the protozoan parasite, *Perkinsus marinus*, of the oyster, *Crassostrea virginica*. *Exp. Parasitol.* **95**, 240–251. (doi:10.1006/expr.2000.4533)
23. Schellander FA, Headington JT. 1974 The stratum corneum—some structural and functional correlates. *Br. J. Dermatol.* **91**, 507–515. (doi:10.1111/j.1365-2133.1974.tb12938.x)
24. Schätzlein A, Cevc G. 1998 Non-uniform cellular packing of the stratum corneum and permeability barrier function of intact skin: a high-resolution confocal laser scanning microscopy study using highly deformable vesicles (Transfersomes). *Br. J. Dermatol.* **138**, 583–592. (doi:10.1046/j.1365-2133.1998.02166.x)
25. Bligh EG, Dyer WJ. 1959 A rapid method of total lipid extraction and purification. *Can. J. Biochem. Physiol.* **37**, 911–917. (doi:10.1139/o59-099)
26. Abrams K, Harvell JD, Shriner D, Wertz P, Maibach H, Maibach HI, Rehfeld SJ. 1993 Effect of organic solvents on *in vitro* human skin water barrier function. *J. Invest. Dermatol.* **101**, 609–613. (doi:10.1111/1523-1747.ep12366068)
27. Wertz PW, Kremer M, Squier CA. 1992 Comparison of lipids from epidermal and palatal stratum corneum. *J. Invest. Dermatol.* **98**, 375–378. (doi:10.1111/1523-1747.ep12499809)
28. Toole GO, Kaplan HB, Kolter R. 2000 Biofilm formation as microbial development. *Annu. Rev. Microbiol.* **54**, 49–79. (doi:10.1146/annurev.micro.54.1.49)
29. Chung KK, Schumacher JF, Sampson EM, Burne RA, Antonelli PJ, Brennan AB. 2007 Impact of engineered surface microtopography on biofilm formation of *Staphylococcus aureus*. *Biointerphases* **2**, 89–94. (doi:10.1116/1.2751405)
30. Standard A. 2002 B46. 1 (2002) Surface Texture, surface roughness, waviness and lay. *Am. Soc. Mech. Eng. An Am. Natl. Stand.* **2002**, 1–98.
31. Kaplan JB. 2010 Biofilm dispersal: mechanisms, clinical implications, and potential therapeutic uses. *J. Dent. Res.* **89**, 205–218. (doi:10.1177/0022034509359403)
32. Rabionet M, Gorgas K, Sandhoff R. 2014 Ceramide synthesis in the epidermis. *Biochim. Biophys. Acta - Mol. Cell Biol. Lipids* **1841**, 422–434. (doi:10.1016/j.bbalip.2013.08.011)
33. Cho HJ, Chung BY, Lee HB, Kim HO, Park CW, Lee CH. 2012 Quantitative study of stratum corneum ceramides contents in patients with sensitive skin. *J. Dermatol.* **39**, 295–300. (doi:10.1111/j.1346-8138.2011.01406.x)
34. Monteiro JM *et al.* 2015 Cell shape dynamics during the staphylococcal cell cycle. *Nat. Commun.* **6**, 8055. (doi:10.1038/ncomms9055)
35. Herman-Bausier P, Valotteau C, Pietrocola G, Rindi S, Alsteens D, Foster TJ, Speziale P, Dufrêne YF. 2016 Mechanical strength and inhibition of the *Staphylococcus aureus* collagen-binding protein Cna. *MBio* **7**, e01529-16. (doi:10.1128/mBio.01529-16)
36. Lee JH, Kaplan JB, Lee WY. 2008 Microfluidic devices for studying growth and detachment of *Staphylococcus epidermidis* biofilms. *Biomed. Microdevices* **10**, 489–498. (doi:10.1007/s10544-007-9157-0)
37. Whitehead KA, Colligon J, Verran J. 2005 Retention of microbial cells in substratum surface features of micrometer and sub-micrometer dimensions. *Colloids Surf. B Biointerfaces* **41**, 129–138. (doi:10.1016/j.colsurfb.2004.11.010)
38. Boyd RD, Verran J, Jones MV, Bhakoo M. 2002 Use of the atomic force microscope to determine the effect of substratum surface topography on bacterial adhesion. *Langmuir* **18**, 2343–2346. (doi:10.1021/la011142p)
39. Kong HH *et al.* 2012 Temporal shifts in the skin microbiome associated with disease flares and treatment in children with atopic dermatitis. *Genome Res.* **22**, 850–859. (doi:10.1101/gr.131029.111)
40. Dussaud AD, Adler PM, Lips A. 2003 Liquid transport in the networked microchannels of the skin surface. *Langmuir* **19**, 7341–7345. (doi:10.1021/la034235a)
41. Zhang Q, Flach CR, Mendelsohn R, Mao G, Pappas A, Mack MC, Walters RM, Southall MD. 2015 Topically applied ceramide accumulates in skin glyphs. *Clin. Cosmet. Investig. Dermatol.* **8**, 329.
42. Sauer K, Camper A, Ehrlich G, Costerton J, Davies D. 2002 *Pseudomonas aeruginosa* displays multiple phenotypes during development as a biofilm. *J. Bacteriol.* **184**, 1140–1154. (doi:10.1128/JB.184.4.1140)
43. Davies DG, Marques CNH. 2009 A fatty acid messenger is responsible for inducing dispersion in microbial biofilms. *J. Bacteriol.* **191**, 1393–1403. (doi:10.1128/JB.01214-08)
44. Fredricks DN. 2001 Microbial ecology of human skin in health and disease. *J. Investig. Dermatol. Symp. Proc.* **6**, 167–169. (doi:10.1046/j.0022-202x.2001.00039.x)
45. Bateman BT, Donegan NP, Jarry TM, Palma M, Cheung AL. 2001 Evaluation of a tetracycline-inducible promoter in *Staphylococcus aureus in vitro* and *in vivo* and its application in demonstrating the role of *sigB* in microcolony formation. *Infect. Immun.* **69**, 7851–7857. (doi:10.1128/IAI.69.12.7851-7857.2001)
46. Cassat J *et al.* 2006 Transcriptional profiling of a *Staphylococcus aureus* clinical isolate and its isogenic *agr* and *sarA* mutants reveals global differences in comparison to the laboratory strain RN6390. *Microbiology* **152**, 3075–3090. (doi:10.1099/mic.0.29033-0)
47. Sauer K, Steczko J, Ash SR. 2009 Effect of a solution containing citrate/methylene blue/parabens on *Staphylococcus aureus* bacteria and biofilm, and comparison with various heparin solutions. *J. Antimicrob. Chemother.* **63**, 937–945. (doi:10.1093/jac/dkp060)
48. Henry-Stanley MJ, Hess DJ, Wells CL. 2014 Aminoglycoside inhibition of *Staphylococcus aureus* biofilm formation is nutrient dependent. *J. Med. Microbiol.* **63**, 861–869. (doi:10.1099/jmm.0.068130-0)
49. Wells CL, Henry-Stanley MJ, Barnes AMT, Dunny GM, Hess DJ. 2011 Relation between antibiotic susceptibility and ultrastructure of *Staphylococcus aureus* biofilms on surgical suture. *Surg. Infect. (Larchmt).* **12**, 297–305. (doi:10.1089/sur.2010.104)
50. Kligman AM, Christophers E. 1963 Preparation of isolated sheets of human stratum corneum. *Arch. Dermatol.* **88**, 702–705. (doi:10.1001/archderm.1963.01590240026005)
51. Warner RR, Boissy YL, Lilly NA, Spears MJ, Mckillop K, Marshall JL, Stone KJ. 1999 Water disrupts stratum corneum lipid lamellae: damage is similar to surfactants. *J. Invest. Dermatol.* **113**, 960–966. (doi:10.1046/j.1523-1747.1999.00774.x)
52. Schaefer H, Redelmeier TE. 1996 The composition and structure of the stratum corneum. In *Skin barrier: principles of percutaneous absorption*, pp. 43–86. Basel, Switzerland: S. Karger AG.
53. Anderson RL, Cassidy JM. 1973 Variations in physical dimensions and chemical composition of human stratum corneum. *J. Invest. Dermatol.* **61**, 30–32. (doi:10.1111/1523-1747.ep12674117)
54. Caussin J, Gooris GS, Janssens M, Bouwstra JA. 2008 Lipid organization in human and porcine stratum corneum differs widely, while lipid mixtures with porcine ceramides model human stratum corneum lipid organization very closely. *Biochim. Biophys. Acta* **1778**, 1472–1482. (doi:10.1016/j.bbamem.2008.03.003)
55. Liu X, German GK. 2015 The effects of barrier disruption and moisturization on the dynamic drying mechanics of human stratum corneum. *J. Mech. Behav. Biomed. Mater.* **49**, 80–89. (doi:10.1016/j.jmbbm.2015.04.017)
56. Style RW, Boltyanskiy R, German GK, Hyland C, MacMinn CW, Mertz AF, Wilen LA, Xu Y, Dufresne ER. 2014 Traction force microscopy in physics and biology. *Soft Matter* **10**, 4047–4055. (doi:10.1039/c4sm00264d)
57. German GK, Engl WC, Pashkovski E, Banerjee S, Xu Y, Mertz AF, Hyland C, Dufresne ER. 2012 Heterogeneous drying stresses in stratum corneum. *Biophys. J.* **102**, 2424–2432. (doi:10.1016/j.bpj.2012.04.045)
58. Marques CNH, Craver SA. 2015 Quantification of respiratory activity in biofilms. *Bio-protocol* **5**, e1591.
59. Andrews JM. 2001 Determination of minimum inhibitory concentrations. *J. Antimicrob. Chemother.* **48**, 5–16. (doi:10.1093/jac/48.suppl_1.5)
60. Dever LL, Jorgensen JH, Barbour AG. 1992 *In vitro* antimicrobial susceptibility testing of *Borrelia burgdorferi*: a microdilution MIC method and time-kill studies. *J. Clin. Microbiol.* **30**, 2692–2697.